Journal of Solid State Chemistry **156,** 286–291 (2001)
doi:10.1006/jssc.2000.8990, available online at http://www.idealibrary.com on IDEAL®

In Situ XAFS Analysis of Li(Mn, M)$_2$O$_4$ (M = Cr, Co, Ni) 5 V Cathode Materials for Lithium-Ion Secondary Batteries

Yasuko Terada,*[,1] Kenji Yasaka,* Fumishige Nishikawa,† Tokuzo Konishi,‡ Masaki Yoshio,§ and Izumi Nakai*

*Department of Applied Chemistry, Faculty of Science, Science University of Tokyo, Kagurazaka, Shinjuku, Tokyo 162-8601, Japan; †Battery Development Laboratory, Asahi Chemical Industry, Co., Ltd., Yako, Kawasaki, Kanagawa 210-0863, Japan; ‡Analytical Research Laboratory, Asahi Chemical Industry, Co., Ltd., Samejima, Fuji, Shizuoka 416-8501, Japan; and §Department of Applied Chemistry, Faculty of Science and Engineering, Saga University, Honjyo, Saga 840-8502, Japan

Received November 2, 1999; in revised form September 2, 2000; accepted October 6, 2000

Chemical states and structural changes accompanying the electrochemical Li deintercalation of Li$_{1-x}$(Mn, M)$_2$O$_4$ (M = Cr, Co, Ni) were studied by the *in situ* X-ray absorption fine structure (XAFS) technique. The X-ray absorption near-edge structures (XANES) of Mn and M as a function of x showed that the high voltage (~ 5 V) in the cathode materials of an Li secondary battery is due to the oxidation of M^{3+} to M^{4+} (M = Cr, Co) and M^{2+} to M^{4+} (in the case of M = Ni), while the origin of the low voltage (3.9–4.3 V) can be ascribed to the oxidation of Mn^{3+} to Mn^{4+}. The extended X-ray absorption fine structure (EXAFS) analysis of Li$_{1-x}$(Mn, Ni)$_2$O$_4$ revealed that Ni^{2+} is oxidized to Ni^{4+} via the Ni^{3+} state with a Jahn–Teller distorted Ni^{3+}–O octahedron.

***Key Words:* *in situ* XAFS analysis; Li secondary battery; Li$_{1-x}$(Mn, M)$_2$O$_4$ (M = Cr, Co, Ni); Jahn–Teller distortion.**

INTRODUCTION

Much attention has been focused on the LiMn$_2$O$_4$ spinel because of its economic and environmental advantages over LiCoO$_2$, which is currently used as a cathode material for lithium ion secondary batteries in commercial batteries (1–3). However, there are several problems that remain to be solved, such as capacity fading under high temperature, before this new material can be used in practical applications. To prevent the lowering of cyclic performance with capacity fading, many studies have been devoted to stabilizing the spinel structure by substituting metal ions such as Mg, Al, Cr, Fe, Ni, and Co for the Mn^{3+} ion (4–7). Recently, several groups have discovered that Li(Mn, M)$_2$O$_4$ (M = Cr, Fe, Ni, Co, Cu) cathode materials exhibit a nearly 5 V operating voltage after reaching the 4 V plateau (7–11). The oxidation states of the dopant metals, M, in the initial stage have been experimentally revealed to be Cr^{3+}, Co^{3+}, Ni^{2+}, and Fe^{3+} by means of electron energy loss spectroscopy (8), X-ray photoemission spectroscopy (9), and Mössbauer spectroscopy (7). However, the oxidation mechanisms of the dopant metals at the 5 V region remained to be elucidated. The X-ray absorption fine structure (XAFS) technique is most suitable for examining structural variations in the transition metal atoms during the charge–discharge process. This method allows us to obtain information about the local structure and electronic structure of the electrode materials at any deintercalation–intercalation stage without disassembling the cell. We have already studied the structural changes of LiCoO$_2$, LiNiO$_2$, Li(Co, Ni)O$_2$, and LiMn$_2$O$_4$ with electrochemical Li deintercalation using transmission *in situ* XAFS cells, and we have clarified the related mechanisms (12–14).

The present study was conducted to reveal variations in the chemical states and the local structure of the Mn and substituent metals, M (M = Cr, Co, Ni), in Li$_{1-x}$(Mn, M)$_2$O$_4$ as a function of the Li content by *in situ* XAFS analysis. In particular, detailed behavior related to variations in the Ni–O$_6$ octahedra in Li$_{1-x}$(Mn, Ni)$_2$O$_4$ during the charge process was clarified by analyzing EXAFS (extended X-ray absorption fine structure) oscillations.

EXPERIMENTAL

The partially substituted Mn spinels LiMn$_{1.25}$Cr$_{0.75}$O$_4$, LiMn$_{1.71}$Co$_{0.29}$O$_4$, and LiMn$_{1.69}$Ni$_{0.31}$O$_4$ for *in situ* XAFS measurements were prepared by solid-state reactions as previously reported (15). The chemical compositions of the synthesized materials were determined by ICP analysis. The LiMn$_{1.6}$Ni$_{0.4}$O$_4$ were synthesized by solid-state reactions in order to obtain charge–discharge cycling performance. The

[1]To whom correspondence should be addressed. Fax: +81-3-3235-2214. E-mail: yterada@ch.kagu.sut.ac.jp.

0022-4596/01 $35.00

structures of these compounds were identified using the X-ray powder diffraction technique.

The electrochemical cells were prepared to evaluate the electrochemical properties of the products. The cathode consisted of active material and a conducting binder (acetylene black and PTFE composite). The electrolyte composition was 1 M $LiPF_6$ in ethylene carbonate (EC): dimethyl carbonate (DMC) (1 : 2 in volume) in all electrochemical measurements. The charge–discharge curves were measured using two-electrode electrochemical cells at a constant current density of 0.5 mA/cm^2.

The *in situ* XAFS cells incorporated a thin film cathode, a liquid electrolyte, and a lithium foil anode. Details of the cell were described in our previous paper (16). Samples as references for metal valences were prepared by mixing the powder samples with a BN powder to form disks. Cr, Mn, Co, and Ni K-XAFS spectra were measured by the transmission mode at various stages of the charge process. The measurements were carried out at BL-7C and 12C, Photon Factory (PF), High Energy Accelerator Research Organization (KEK), Tsukuba, Japan. An Si(111) double-crystal monochromator was used, and the intensities of the incident and transmitted X-rays were measured by the ion chamber detectors at room temperature. The sample weights of the cathodes were adjusted in order to maintain an optimum thickness for the measurements in the transmission mode suitable for each target element. The cells were charged to a desired voltage at a constant current, then kept in a resting condition for ca. 40 min. The cathode composition, the sample weight per unit area, and the constant current value for the XAFS measurement are shown in Table 1. The EXAFS data were analyzed by conventional methods using REX2 data analysis software (17). The EXAFS oscillation, $\chi(k)$, was extracted from the spectrum using the Victreen function and the cubic spline technique. The Fourier transforms (FT) of $k^3\chi(k)$ yielded the radial distribution functions, which are not corrected for the phase shift. Fourier filtering and subsequent curve-fitting analysis were used to reveal the structural parameters. The theoretical parameters of the backscattering amplitude and phase shifts used in the curve fitting analysis were calculated by FEFF 8 (18). The ordinate scale of the XANES spectra was normalized at 500 eV above the absorption edge, where the differences in the EXAFS oscillations among the spectra were negligible. The K-edge energies of all the target elements were defined as the energy at the half height of the absorption edge, and their chemical shifts are represented by the energy difference in the K-edge energy from the initial state ($x = 0$).

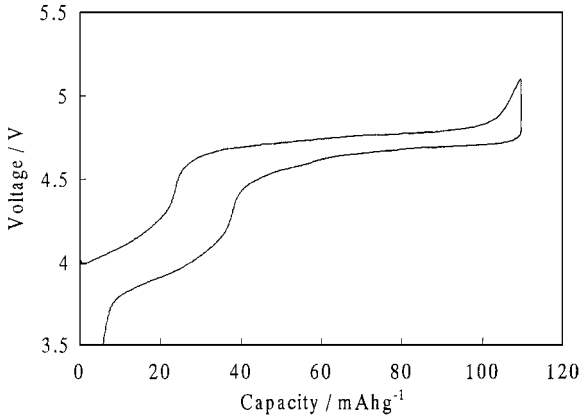

FIG. 1. Charge–discharge curves at the third cycle for the Li/$LiMn_{1.6}Ni_{0.4}O_4$ cell cycled in EC:DMC (1:2)/1M $LiPF_6$ at a current density of 0.5 mA/cm^2 within the voltage limits of 3.5 to 5.1 V.

RESULTS AND DISCUSSION

Figure 1 shows the charge–discharge curves measured at the third cycle of the $LiMn_{1.6}Ni_{0.4}O_4$ cell with voltage limits of 3.5 to 5.1 V (vs Li metal). The initial discharge capacity was 103.9 mAh/g. Two major plateaus appear in the curves. The plateau near 4.3 V is very narrow because the average valence of manganese is close to Mn^{4+} in this cathode composition. The charge–discharge curves of the other materials Li(Mn, M)$_2O_4$ (M = Cr, Co) also showed two plateaus near 4.3 and 5 V similar to $LiMn_{1.6}Ni_{0.4}O_4$.

The Mn K-XANES spectra of $Li_{1-x}Mn_{1.71}Co_{0.29}O_4$ measured as a function of x are shown in Fig. 2. The Li concentrations $(1 - x)$ were estimated from the known cathode masses and the total charge. As can be seen from Fig. 2, the Mn K-edge absorption energy shifts to the higher energy side with increases in x, indicating that Mn^{3+} is oxidized to Mn^{4+} with the Li deintercalation. The measured chemical shift of the Mn K-edge spectra for Li_{1-x}(Mn, M)$_2O_4$ is plotted as a function of x in Fig. 3. The oxidation of Mn is primarily responsible for the 4 V plateau region independent of the kind of substituent metals. The total chemical shift of the Mn K-edge is the largest for $Li_{1-x}Mn_{1.71}Co_{0.29}O_4$ (0.9 eV), while the chemical shifts are almost the

TABLE 1
Cathode Composition, the Weight of the Sample per Unit Area, and the Constant Current Value for the *in Situ* XAFS Measurements

Sample composition	$LiMn_{1.25}Cr_{0.75}O_4$	$LiMn_{1.69}Ni_{0.31}O_4$		$LiMn_{1.71}Co_{0.29}O_4$	
Target element	Mn, Cr	Mn	Ni	Mn	Co
Weight (mg/0.79 cm^2)	5.6	3.72	23.7	3.64	28.0
Current (mA)	0.2	0.2	0.5	0.2	0.5

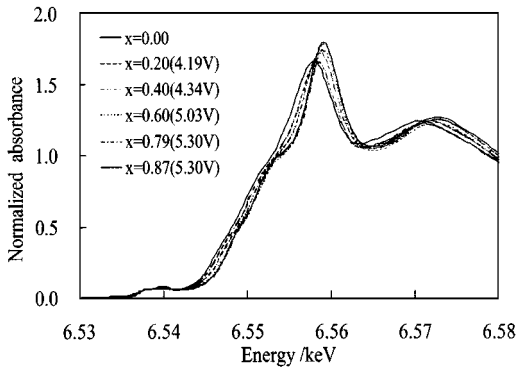

FIG. 2. Mn K-XANES spectra of $Li_{1-x}Mn_{1.71}Co_{0.29}O_4$ measured as a function of Li content (x).

same for $Li_{1-x}Mn_{1.25}Cr_{0.75}O_4$ (0.6 eV) and $Li_{1-x}Mn_{1.69}Ni_{0.31}O_4$ (0.5 eV). This difference is due to the difference in the average valence state of Mn at the initial stage of each phase: the nominal oxidation states are calculated to be $+3.58$, $+3.80$, and $+3.78$ for $Li_{1-x}Mn_{1.71}Co_{0.29}O_4$, $Li_{1-x}Mn_{1.25}Cr_{0.75}O_4$, and $Li_{1-x}Mn_{1.69}Ni_{0.31}O_4$, respectively, and Mn is finally oxidized to Mn^{4+} in all cases.

On the other hand, the XANES spectra of the substituent metals show various changes. The Cr, Co, and Ni K-XANES spectra of $Li_{1-x}Mn_{1.25}Cr_{0.75}O_4$, $Li_{1-x}Mn_{1.71}Co_{0.29}O_4$, and $Li_{1-x}Mn_{1.69}Ni_{0.31}O_4$ as a function of x are shown in Figs. 4a–4c, respectively. The XANES spectrum of Cr begins to shift when x exceeds 0.34, but the chemical shift is very small (the total shift is 1.2 eV in Fig. 4a). This shift means that Cr^{3+} in $Li_{1-x}Mn_{1.25}Cr_{0.75}O_4$ is oxidized to a higher chemical state (probably to Cr^{4+}) during the 5 V charging process. The Co K-edge of $Li_{1-x}Mn_{1.71}Co_{0.29}O_4$ shifts to the higher energy side with Li deintercalation, indicating that Co^{3+} is oxidized to Co^{4+} (Fig. 4b), but the spectral changes in shape are different from those of $Li_{1-x}CoO_2$ (12). This result suggests that the local structures of Co are different between $Li_{1-x}Mn_{1.71}Co_{0.29}O_4$ and

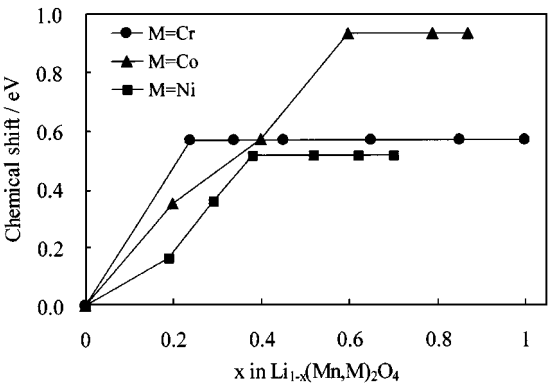

FIG. 3. Composition dependence of the chemical shift for Mn in $Li_{1-x}(Mn, M)_2O_4$ (M = Cr, Ni, Co).

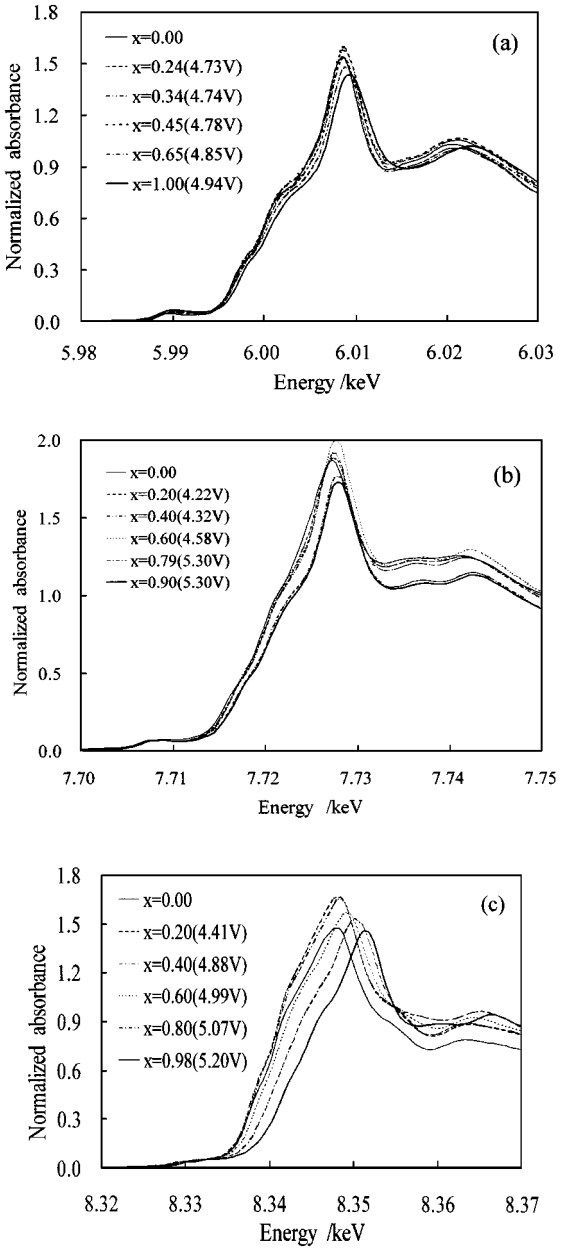

FIG. 4. Variations in the Cr, Co, and Ni K-XANES spectra of (a) $Li_{1-x}Mn_{1.25}Cr_{0.75}O_4$, (b) $Li_{1-x}Mn_{1.71}Co_{0.29}O_4$, and (c) $Li_{1-x}Mn_{1.69}Ni_{0.31}O_4$ during the charge process.

$Li_{1-x}CoO_2$, though both Co are octahedrally coordinated by oxygen atoms. In contrast, the spectrum of Ni in Fig. 4c begins to shift at $x = 0.4$, and the chemical shift is extremely large (the total shift is as large as 4.2 eV in Fig. 5). Because the Ni K-edge energy at $x = 0$ (8.3407 keV) coincides with that of reference Ni^{2+} $(CH_3COO)_2 \cdot H_2O$ (8.3411 keV), the existence of Ni^{2+} in the $LiMn_{1.69}Ni_{0.31}O_4$ spinel is confirmed. Mansour and Melendres have pointed out the linear

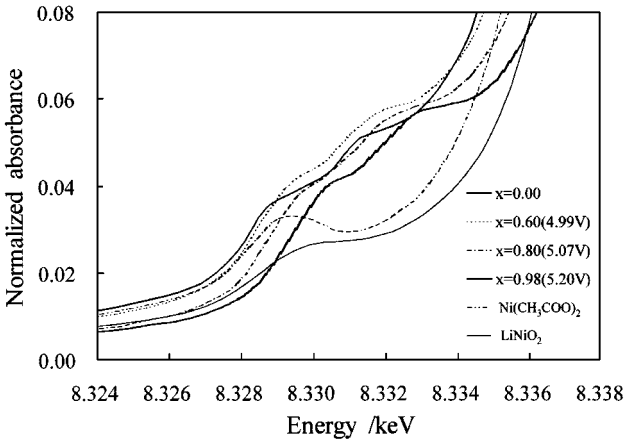

FIG. 5. Normalized XANES of the Ni K-preedge structures of $\cdot H_2O$, $Li_{1-x}Mn_{1.69}Ni_{0.31}O_4$ and $Ni^{2+}(CH_3COO)_2 \cdot H_2O$, and $LiNiO_2$ as reference materials.

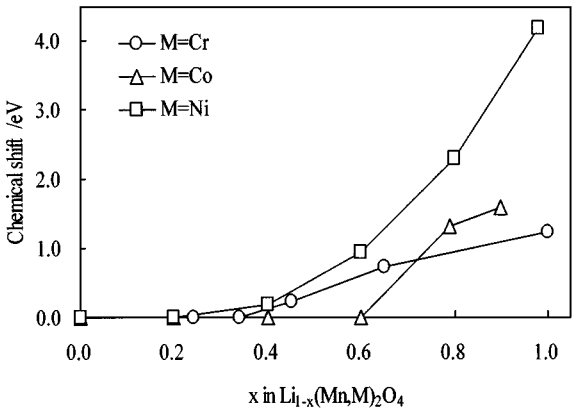

FIG. 6. Composition dependence of the chemical shift for substituent metals (M = Cr, Co, Ni) in Li_{1-x} (Mn, M)$_2O_4$.

relationship between the Ni valency and the Ni K-edge energy for various Ni compounds (19). They have reported that the chemical shift accompanied by the oxidation from Ni^{2+} to Ni^{4+} is 3.7 eV, which is in good agreement with the present result supporting the oxidation of Ni^{2+} to Ni^{4+}. Based on these observations, the charge–discharge curve of $LiMn_{1.6}Ni_{0.4}O_4$ in Fig. 1 can be explained as follows. The plateau at 4.3 V arises from the Mn^{3+}–Mn^{4+} redox pair, and a 4.7 V plateau can be attributed to the oxidation from Ni^{2+} to Ni^{4+}.

The Ni K-XANES spectra of $Li_{1-x}Mn_{1.69}Ni_{0.31}O_4$, $Ni^{2+}(CH_3COO)_2 \cdot H_2O$, and $LiNiO_2$ showed preedge absorption at around 8.33 keV, which is due to the transition from the 1*s* core level to the empty *d* level. These spectra are shown in Fig. 5. The weak intensity of the absorption is due to the absorption being a forbidden transition by dipole selection rules. It is thought that the peak at 8.329 keV of $Ni(CH_3COO)_2 \cdot H_2O$ is associated with a hybridization between O 2*p* and Ni 3*d* orbitals. Similar Ni K-preedge spectra of NiO, α-$Ni(OH)_2$, β-$Ni(OH)_2$, $LiNiO_2$, and $KNiIO_6$ have been reported by Mansour and Melendres (19). These spectra have only one peak, with the peak exhibiting a positive shift with increases in the Ni valency, whereas two peaks are visible for $Li_{1-x}Mn_{1.69}Ni_{0.31}O_4$. These two peaks show a parallel shift with Li deintercalation when x exceeds 0.6. It seems that the Ni ion in the spinel structure has a unique electronic structure.

The relation between the Li deintercalation and the chemical shifts of Cr, Co, and Ni ions are summarized in Fig. 6. The oxidations of the Cr, Co, and Ni ions begin at the 5 V region (above $x = 0.34$ for Cr, $x = 0.6$ for Co, and $x = 0.4$ for Ni). These results also explain the improvements in the cyclic performance of these batteries in the 4V region that occur as a result of the substitution of other metals (M = Cr, Co, Ni) for Mn in $LiMn_2O_4$. All M ions only help to stabilize the spinel structure and do not appear to contribute to the charging in the 4 V region. Actually, it has been reported that Li(Mn, M)$_2O_4$ (M = Cr, Ni, Co) spinels show better cyclic performance than a stoichiometric $LiMn_2O_4$ spinel (6).

The *in situ* EXAFS spectra of the Mn, Co, and Ni K-edges in $Li_{1-x}Mn_{1.71}Co_{0.29}O_4$ and $Li_{1-x}Mn_{1.69}Ni_{0.31}O_4$ were measured. Fourier transforms (FT) of the k^3-weighted Mn and Ni K-edge EXAFS oscillations of $Li_{1-x}Mn_{1.69}Ni_{0.31}O_4$ are shown as a function of x in Figs. 7a and 7b, respectively. The abscissa axis shows the interatomic distances, which are not corrected for the phase shift, between the absorber atoms M and the coordinated atoms, and the ordinate axis shows the FT magnitude. The peak height of the FT is related to the backscattering of the photoelectrons by the coordinated atoms.

In Fig. 7a, the first peak at around 1.5 Å in FT corresponds to the Mn–O interaction in the first coordination sphere, and the second peak at around 2.5 Å is due to the Mn–(Mn, Ni) interaction in the second coordination sphere. At a greater distance, the peak at around 4.5 Å represents the second Mn or Ni neighbor of the central Mn atom, and the peak at arong 5.0 Å is due to the multiscattering of Mn being twice the distance of the nearest Mn or Ni atoms. The amplitudes of the Mn–O and Mn–(Mn, Ni) peaks increase monotonously with the Li intercalation. Shiraishi *et al.* have previously observed this phenomena and have reported that in their study the low peak height could be attributed to the coexistence of Mn^{3+} and Mn^{4+} ions at the 16*d* site of the spinel structure in $Li_{1-x}Mn_2O_4$ with two different Mn–O_6 coordination octahedra (13). In the present case, a slight increase in the Mn–O peak height can be observed with the Li deintercalation because the amount of Mn^{3+} is small in $Li_{1-x}Mn_{1.69}Ni_{0.31}O_4$ compared with stoichiometric $LiMn_2O_4$, where half of the Mn present is Mn^{3+}.

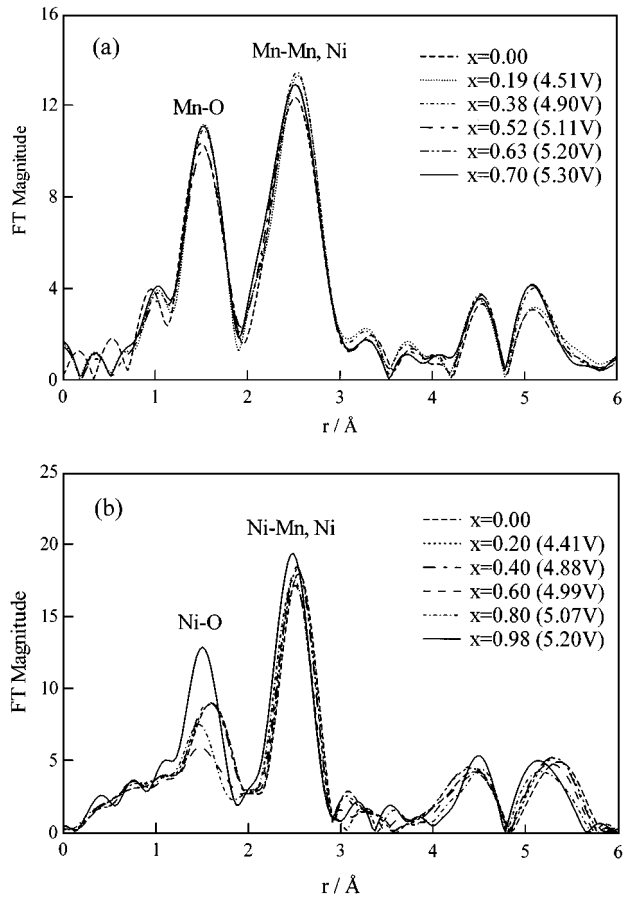

FIG. 7. Fourier transforms of the Mn K-edge (a) and Ni K-edge (b) EXAFS spectra of $Li_{1-x}Mn_{1.69}Ni_{0.31}O_4$ with Li deintercalation (x).

The first and second peaks in Fig. 7b represent the Ni–O and Ni–(Mn, Ni) interactions, respectively. The intensities of the Ni–(Mn, Ni) peaks increase with the Li deintercalation; however, the Ni–O peak height shows a peculiar variation. The height of the Ni–O peak begins to decrease when x exceeds 0.4, and then reaches a minimum at $x = 0.6$. Then, the Ni–O peak increases significantly with the deintercalation of Li. An extraordinarily small Ni–O peak has also been observed in $LiNiO_2$ (12). It has been reported that such a peak is caused by the Jahn–Teller distortion of the Ni^{3+}–O_6 octahedron (12). Our results also suggest that the small Ni–O peaks can be ascribed to the distorted Ni^{3+}–O octahedron from the true octahedral coordination due to the Jahn–Teller effect. Specifically, it appears that Ni^{2+} is first oxidized to the low-spin Ni^{3+}, which is the d^7 Jahn–Teller ion; then, when x exceeds 0.6, Ni^{3+} starts to oxidize to Ni^{4+}.

To evaluate the distortion of the Ni–O_6 octahedra in $Li_{1-x}Mn_{1.69}Ni_{0.31}O_4$, inverse Fourier transforms were performed on the first Ni–O peaks of the FT in Fig. 7b. The resulting $\chi(k)$ functions were then analyzed using iterative nonlinear least-square curve fitting techniques with the parameters calculated by FEFF8 (18). The curve fitting was carried out using two models. The first model assumed the presence of two different Ni–O_6 coordination octahedra ($2 + 4$ model), and the second assumed uniform single Ni–O_6 octahedra with six equal Ni–O distances. The calculated structural parameters are given in Table 2. As is evident from Table 2, the $(2+4)$ model gave much better fitting results for $x = 0.6$ and 0.8 in $Li_{1-x}Mn_{1.69}Ni_{0.31}O_4$ than the equidistant model, which yielded a significantly lower R factor ($= \Sigma(k^3\chi_{obs} - k^3\chi_{calc})^2/\Sigma(k^3\chi_{obs})^2$) and a reasonable coordination number (N) and Debye–Waller factors (σ). The obtained Ni–O1 and Ni–O2 distances, 1.99 and 1.91 Å, are close to the literature data for Ni^{2+}–O, 2.07 Å and Ni^{3+}–O (low-spin), 1.94 Å, for $x = 0.6$ phase (20). Similarly the Ni–O1 and Ni–O2 distances, 1.92 and 1.86 Å, are in good agreement with the reported values for Ni^{3+}–O, 1.94 Å, and Ni^{4+}–O, 1.86 Å, for the $x = 0.8$ phase (20). Consequently, it seems reasonable to conclude that Ni in the $Li_{1-x}Mn_{1.69}Ni_{0.31}O_4$ spinel contains two distinct Ni–O_6 octahedra such as Ni^{2+}–O_6, Ni^{3+}–O_6 for the $x = 0.6$ phase and Ni^{3+}–O_6, Ni^{4+}–O_6 for the $x = 0.8$ phase. This is the first observation of a dynamic change in oxidation state during the oxidation of Ni^{2+} to Ni^{4+} with

TABLE 2
A Comparison of the Structure Parameters in $Li_{1-x}Mn_{1.69}Ni_{0.31}O_4$ Obtained from the Curve-Fitting Analysis Assuming the (2 + 4) and 6 Equidistant Ni–O Coordination Models

	(2 + 4) Ni–O coordination model					6 equidistant Ni–O coordination model			
x	Coordination atom	N	r/ Å	σ/ Å	R	Coordination atom	r/ Å	σ/ Å	R
0.6	O1	1.92	1.99	0.091	4.28	O	1.96	0.104	5.16
	O2	4.11	1.91	0.080					
0.8	O1	4.06	1.92	0.089	2.37	O	1.87	0.083	4.70
	O2	1.94	1.86	0.063					
0						O	2.00	0.092	3.94
0.98						O	1.86	0.072	2.53

Note. N: coordination number of oxygen; r: Ni–O distance; σ: Debye–Waller factor; R: $\Sigma(k^3\chi_{obs} - k^3\chi_{calc})^2/\Sigma(k^3\chi_{obs})^2$.

Li deintercalation. On the other hand, for the initial and final phases ($x = 0$ and 0.98), a uniform Ni–O_6 octahedron with equal Ni–O distances gives good fitting results, as shown in Table 2. The calculated Ni–O distance for Ni^{2+}–O_6 octahedra is 2.00 Å at $x = 0$, and that for Ni^{4+}–O_6 is 1.86 Å at $x = 0.98$. Thus, it is clear from the variations in the Ni–O octahedral distances that Ni^{2+} is at first oxidized to Ni^{3+}, and then finally reaches Ni^{4+} during the Li deintercalation process.

SUMMARY

The *in situ* XAFS spectra of $Li_{1-x}(Mn, M)_2O_4$ (M = Cr, Co, Ni) were measured to reveal the mechanism of the oxidation reaction during Li deintercalation. The oxidation of Mn^{3+} to Mn^{4+} is associated with the charge process at low voltage (3.9–4.3 V), and the high voltage (near 5 V) is due to the oxidations of Cr^{3+}, Co^{3+}, and Ni^{2+}. It is found from the Ni K-edge XAFS analysis that Ni in $Li_{1-x}Mn_{1.69}Ni_{0.31}O_4$ experiences three distinct valence states with the Li deintercalation, Ni^{2+}, Ni^{3+}, and Ni^{4+}. The average Ni^{2+}–O, Ni^{3+}–O, and Ni^{4+}–O octahedral distances were found to be 2.00, 1.92, and 1.86 Å, respectively. The theoretical Ni–O distances calculated from the ionic radii (20) have been found to be 2.07 for Ni^{2+}–O, 1.94 for Ni^{3+}–O (low-spin state), and 1.86 Å for Ni^{4+}–O, which is in fair agreement with the present results. The electrochemical Li deintercalation first causes the oxidation of Ni^{2+} to Ni^{3+}, Ni^{3+} is then oxidized to Ni^{4+}. Thus, a dynamical change in the Ni oxidation state with the Li deintercalation can be elucidated experimentally for the first time. A detailed EXAFS analysis of $Li_{1-x}Mn_{1.71}Co_{0.29}O_4$ is now in progress.

ACKNOWLEDGMENTS

The authors thank Mrs. Y. Shiraishi, H. Kitamura, and Y. Nishiwaki of the Science University of Tokyo for their help in carrying out the XAFS measurements. The XAFS experiments were carried out under the approval of the PF program Advisory Committee (Proposal No. 98G338).

REFERENCES

1. M. M. Thackeray, W. I. F. David, P. G. Bruce, and J. B. Goodenough, *Mater. Res. Bull.* **18,** 461 (1983).
2. R. J. Gummow, A. Kock, and M. M. Thackeray, *Solid State Ionics* **69,** 59 (1994).
3. K. Miura, A. Yamada, and M. Tanaka, *Electrochim. Acta* **41,** 24 (1996).
4. N. Hayashi, H. Ikuta, and M. Wakihara, *J. Electrochem. Soc.* **146,** 1351 (1999).
5. D. Song, H. Ikuta, T. Uchida, and M. Wakihara, *Solid State Ionics* **117,** 151 (1999).
6. Li Gouhua, H. Ikuta, T. Uchida, and M. Wakihara, *J. Electrochem. Soc.* **143,** 178 (1996).
7. H. Kawai, M. Nagata, M. Tabuchi, H. Tukamoto, and A. R. West, *Chem. Mater.* **10,** 3266 (1998).
8. C. Sigala, A. Verbaere, J. L. Mansot, D. Guyomard, Y. Piffard, and M. Tournoux, *J. Solid State Chem.* **132,** 372 (1997).
9. K. Amine, H. Tukamoto, H. Yasuda, and Y. Fujita, *J. Electrochem. Soc.* **143,** 1607 (1996).
10. H. Kawai, M. Nagata, H. Tukamoto, and A. R. West, *J. Mater. Chem.* **8,** 837 (1998).
11. Y. Ein-Eli and W. F. Howard, *J. Electrochem. Soc.* **144,** L205 (1997).
12. I. Nakai, K. Takahashi, Y. Shiraishi, T. Nakagome, and F. Nishikawa, *J. Solid State Chem.* **140,** 145 (1998).
13. Y. Shiraishi, I. Nakai, T. Tsubata, T. Himeda, and F. Nishikawa, *J. Solid State Chem.* **133,** 587 (1997).
14. I. Nakai and T. Nakagome, *Electrochem. Solid State Lett.* **1,** 259 (1998).
15. H. Kurimoto, K. Shizuoka, T. Murakami, Y. Xia, H. Nakamura, and M. Yoshio, *J. Electrochem. Soc.* **142,** 2178 (1995).
16. I. Nakai, Y. Shiraishi, and F. Nishikawa, *Spectrochim. Acta B* **54,** 143 (1999).
17. Rigaku EXAFS analysis software, REX2, Cat. No. 2612S211, RIGAKU Co., 1996.
18. A. L. Ankudinov, B. Ravel, J. J. Rehr, and S. D. Conradson, *Phys. Rev. B* **58,** 7565 (1998).
19. A. N. Mansour and C. A. Melendres, *J. Phys. Chem. A* **102,** 65 (1998).
20. R. D. Shannon, *Acta Crystallogr. A* **32,** 751 (1976).